UNIVERSITY OF
BATH

University of Bath

Reversible Magnesium and Aluminium-ions Insertion in Cation-Deficient Anatase TiO₂

Toshinari Koketsu[a†] Jiwei Ma[b,c†,*], Benjamin J. Morgan[d], Monique Body[e], Christophe Legein[e], Walid Dachraoui[c,f], Mattia Giannini[f,g], Arnaud Demortiere[c,f,g], Mathieu Salanne[b,c], François Dardoize[b], Henri Groult[b], Olaf J. Borkiewicz[h], Karena W. Chapman[h], Peter Strasser[a,*], and Damien Dambournet[b,c,*]

[a]*The Electrochemical Energy, Catalysis, and Materials Science Laboratory, Department of Chemistry, Chemical Engineering Division, Technical University Berlin, 10623 Berlin, Germany.*

[b]*Sorbonne Universités, UPMC Univ Paris 06, CNRS UMR 8234, Laboratoire PHENIX, 4 place Jussieu, F-75005 Paris, France.*

[c]*Réseau sur le Stockage Electrochimique de l'Energie (RS2E), FR CNRS 3459, France.*

[d]*Department of Chemistry, University of Bath, BA2 7AY Bath, United Kingdom.*

[e]*Université Bretagne Loire, Université du Maine, UMR CNRS 6283, Institut des Molécules et des Matériaux du Mans (IMMM), Avenue Olivier Messiaen, 72085 Le Mans Cedex 9, France.*

[f]*Laboratoire de Réactivité et Chimie des Solides, CNRS UMR 7314, Université de Picardie Jules Verne, 33 rue Saint Leu, 80039 Amiens Cedex, France.*

[g]*ALISTORE-European Research Institute, FR CNRS 3104, 80039 Amiens, France.*

[h]*X-ray Science Division, Advanced Photon Source, Argonne National Laboratory, 9700 South Cass Avenue, Argonne, Illinois 60439, United States.*

[†]*These authors contributed equally to this work.*

[*]To whom correspondence should be addressed. E-mail address: jiwei.ma@upmc.fr (J.M.), pstrasser@tu-berlin.de (P.S.), damien.dambournet@upmc.fr (D.D.)

Abstract. In contrast to monovalent lithium or sodium ions, the reversible insertion of multivalent ions such as Mg^{2+} and Al^{3+} into electrode materials remains an elusive goal. Here, we demonstrate a new strategy to achieve reversible Mg^{2+} and Al^{3+} insertion in anatase TiO_2, achieved through aliovalent doping, to introduce a large number of titanium vacancies that act as intercalation sites. We present a broad range of experimental and theoretical characterizations that show a preferential insertion of multivalent ions into titanium vacancies, allowing a much greater capacity to be obtained compared to pure TiO_2. This result highlights the possibility to use the chemistry of defects to unlock the electrochemical activity of known materials providing a new strategy for the chemical design of materials for practical multivalent batteries.

Rechargeable batteries are increasingly used across a broad range of applications, from electric vehicles, to grid storage and load-leveling for primary renewable energy sources.[1] At present, the continually increasing demands for energy storage are largely met by lithium-ion (Li-ion) batteries.[2,3] A global transition from fossil fuels to low greenhouse-gas-emission energy sources, however, will require diverse energy-storage technologies, each appropriate for its target application.[1] Batteries are expected to play a central role in any future global portfolio of energy storage technologies. In particular, it is expected that "beyond lithium" chemistries will allow batteries to be developed and implemented for applications not presently addressed by Li-ion technologies. Within this area, batteries based on multivalent ions are particularly attractive for large scale energy storage applications because of their superior theoretical volumetric energy densities. The development of multivalent batteries, however, still faces scientific challenges related to matching electrolyte properties with specific operating voltage windows, achieving reversible metal stripping and deposition, and the design of suitable electrode materials.[4-9]

Among multivalent ions, the most promising cations for rechargeable batteries are Earth-abundant, light, and have small ionic radii, such as Mg^{2+} (0.72 Å) and Al^{3+} (0.53 Å).[7,10] Following the pioneering work of Aurbach *et al.*,[5] rechargeable magnesium-ion (Mg-ion) batteries have been considered a promising beyond-lithium-ion candidate. Magnesium metal can be used as an anode without the issues of dendrite formation that complicate Li technologies. Magnesium is abundant in the Earth's crust, has a reduction potential of *ca.* -2.3 V/NHE, and has a higher volumetric capacity than lithium metal.[7,11,12] Despite these promising aspects, the development of rechargeable Mg-ion batteries has been impeded by intrinsic limitations related to intercalation chemistry of Mg^{2+}.[7,13-15] Divalent Mg^{2+} typically

exhibits strong electrostatic interactions with the host lattice, which can cause slow Mg^{2+} diffusion and inhibit reversible intercalation on practical timescales.[13,16] Similar kinetic limitations, again due to strong Coulombic ion–lattice interactions, have hindered other multivalent battery technologies, such as Al-ion. Materials that are electrochemically active towards Li^+ are typically inactive towards multivalent ions. To realize beyond-lithium devices, it is therefore necessary to develop new synthetic strategies for materials that reversibly insert multivalent ions. Here, we report the use of defect engineering to convert electrodes with poor electrochemical activities towards Mg and Al into functionally active electrodes for Mg- and Al-ion batteries. As a proof-of-concept, we demonstrate this strategy using the example parent material anatase-structured TiO_2. This widely studied metal oxide can reversibly intercalate Li^+ ions,[17-20] but does not readily intercalate higher valence Mg^{2+} and Al^{3+} ions.[21-23]

Because Mg and Li ions have comparable ionic radii—0.72 Å and 0.76 Å, respectively—one might expect anatase TiO_2 to readily accommodate magnesium ions. Recent calculations have predicted very similar intercalation energies for Mg^{2+} and Li^+ in anatase TiO_2 in the dilute limit (-1.74 eV and -1.85 eV respectively).[24] Despite favourable thermodynamics, however, stoichiometric anatase shows poor electrochemical activity versus Mg, suggesting kinetic limitations.[21,22] Liu et al.[23] showed that Al^{3+}, which has a smaller ionic radius of 0.53 Å, can be inserted into anatase in aqueous batteries. The extension of this work toward non-aqueous rechargeable batteries, however, remains to be done.

Here, we report how doping anatase TiO_2 to form a large number of charge-compensating titanium vacancies (22 %) greatly improves the electrochemical performance towards Mg and Al. The vacancies act as microstructural voids that readily accommodate Mg^{2+}/Al^{3+}, resulting in materials with greatly enhanced reversible capacities. This work shows that the targeted introduction of defects into electrode materials is a viable approach to engineering electrodes for multivalent batteries.

Titanium vacancies as host sites for multivalent cations: DFT calculations

The effect of introducing titanium vacancies into anatase TiO_2 on intercalation behavior was first probed using density functional theory (DFT). We have previously shown that monovalent-doping (F-, OH-; hereafter denoted F-TiO_2 for sake of clarity) of anatase TiO_2 introduces a large number of charge-compensating Ti vacancies,[20] which preferentially intercalate monovalent ions such as Li. To study the behavior towards intercalation of multivalent ions, we first performed a series of DFT calculations to compare intercalation energies for Li, Mg, and Al in anatase TiO_2 and in F-doped TiO_2. For this we considered two

models for F-TiO$_2$, featuring a single vacancy and a paired-double vacancy, each representative of the local structure observed by solid-state ^{19}F NMR. Our calculated intercalation energies for Li, Mg, and Al at Ti vacancies in F-doped anatase TiO$_2$ versus stoichiometric anatase TiO$_2$ predicts strongly enhanced intercalation for F-doped TiO$_2$. **Figure 1** shows the three possible host sites considered: the interstitial site in stoichiometric anatase, and the single- and double-titanium vacancies in F-doped TiO$_2$.[20] In the Ti vacancy calculations, we considered supercells where oxide ions in equatorial positions around the vacancies were preferentially replaced by fluoride ions, which we have previously shown corresponds to energetically favourable defect configurations.[20] In F-doped TiO$_2$, the F$^-$ dopants substitute for O^{2-} ions, and charge-compensating Ti vacancies are formed, producing a defect ratio of 4 F$^-$ per V_{Ti}. For our DFT calculations our single- and double-vacancy systems have compositions of Ti$_{35}\square_1$O$_{68}$F$_4$ and Ti$_{126}\square_2$O$_{248}$F$_8$.

We calculated the intercalation energies of Li$^+$, Mg^{2+}, and Al^{3+} inserted at an interstitial site (in stoichiometric anatase TiO$_2$), and at the V_{Ti} sites (in F-doped TiO$_2$). In stoichiometric anatase TiO$_2$, these calculations confirm the thermodynamic driving force for the intercalation of multivalent cations is smaller than for than for Li$^+$. The intercalation energies for Li, Mg, and Al are -1.52 eV, -1.02 eV, and -1.25 eV respectively. In F-doped anatase systems, however, all three cations intercalate more readily at titanium vacancy sites, with intercalation energies of -2.92 eV (Li), -3.30 eV (Mg), and -3.13 eV (Al). Significantly, the change in intercalation energy for the multivalent ions is larger than for lithium. From a thermodynamic perspective, therefore, these titanium vacancy sites are predicted to readily intercalate not only lithium, but also multivalent ions. This suggests that the introduction Ti vacancies through targeted aliovalent doping might activate anatase TiO$_2$ towards the intercalation of multivalent ions.
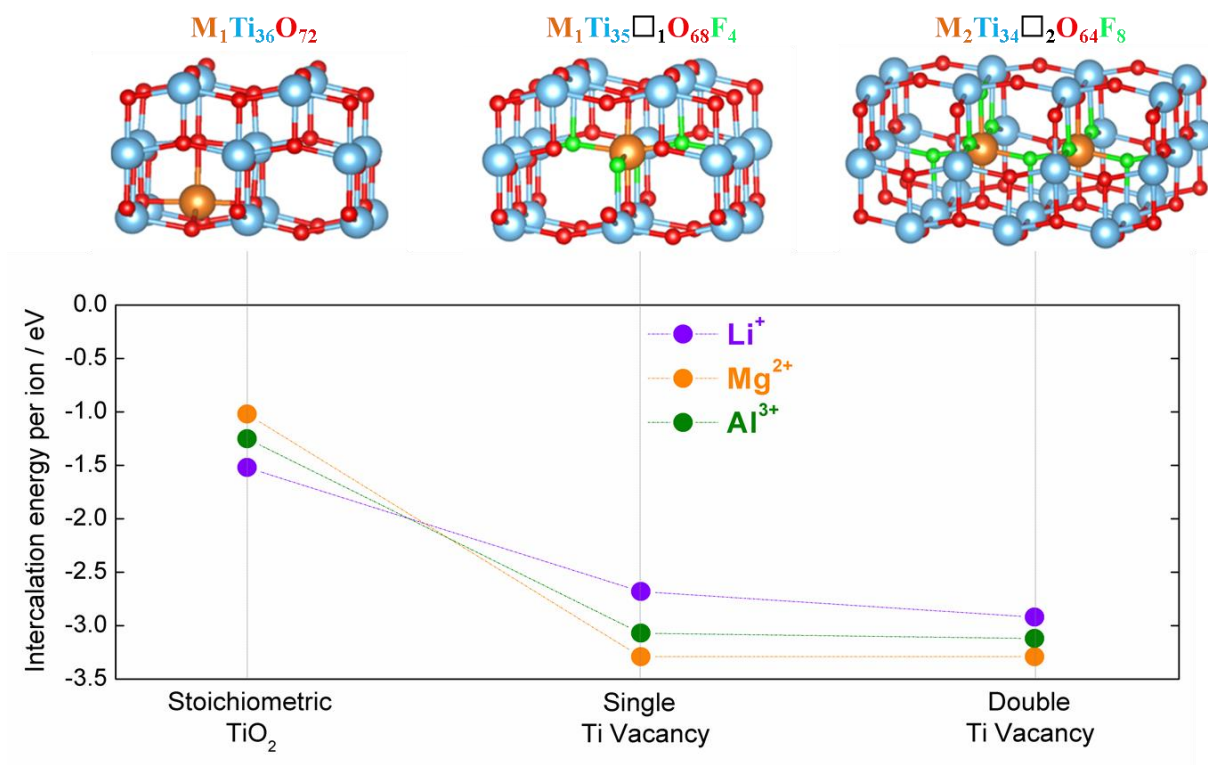
Figure 1. **Titanium vacancies enabling insertion of Mg^{2+} and Al^{3+} in anatase.** DFT calculated intercalation energies for Li, Mg, and Al in anatase TiO_2 and in F-doped TiO_2 (bottom). Corresponding structural representations of the intercalation sites in stoichiometric (defect-free) $Ti_{36}O_{72}$, single vacancy $Ti_{35}\square_1O_{68}F_4$ and double–vacancy $Ti_{126}\square_2O_{248}F_8$ anatase.

Synthesis and electrochemical properties

To test this hypothesis, drawn from our DFT calculations, we synthesized samples with high concentrations of titanium vacancies stabilized in the anatase TiO_2 framework, which is achieved through the partial substitution of oxides ions by monovalent anions, such as fluoride and hydroxide groups.[20,25] The previously reported synthetic strategy produces samples with general chemical formula $Ti_{1-x-y}\square_{x+y}O_{2-4(x+y)}F_{4x}(OH)_{4y}$, where $\square$ represents a cationic vacancy. In this work, we used a compound with 22 % cationic vacancies, corresponding to $Ti_{0.78}\square_{0.22}O_{1.12}F_{0.40}(OH)_{0.48}$ (Figure S1 and Table S1 in Supporting Information).

Atomic resolution images of $Ti_{0.78}\square_{0.22}O_{1.12}F_{0.40}(OH)_{0.48}$ nanocrystals, obtained from an aberration corrected TEM, allow direct visualization of the titanium vacancies (**Figure 2a-e**). The variation in atomic column intensity observed on the high-resolution image (**Figure 2b**) corresponds to a variation in the Ti atomic occupation, and hence points to the presence of vacancies.[26] The intensity variation and dark contrast between atomic columns is emphasized in the colored image and in the line profile in the **Figure 2c**. High-resolution TEM images were calculated (space group I4$_1$/amd) with a Ti atomic occupancy fixed at 78 % with either a

uniform (**Figure 2d**) or random (**Figure 2e**) distribution. The calculated image featuring a random distribution of vacancies is in a good agreement with the experimental image.

The electrochemical activity of $Ti_{0.78}\square_{0.22}O_{1.12}F_{0.40}(OH)_{0.48}$ *vs.* Mg^{2+} ions was evaluated using a three-electrodes Swagelok cell employing magnesium metal as anode and reference electrodes, and $2PhMgCl$-$AlCl_3$/THF solution as the electrolyte (**Figure 2f).** For comparison purpose, we evaluated the electrochemical activity of nanosized formally stoichiometric anatase TiO_2 (Figure S1 and Table S1 in Supporting Information) which gives a reversible capacity of only 25 mAh g^{-1} (0.037 Mg^{2+} per formula unit) confirming the poor intercalation properties. Note that we employed nanoparticles of similar dimension to rule out size effects particularly well established for Li-insertion properties in this compound.[27] $Ti_{0.78}\square_{0.22}O_{1.12}F_{0.40}(OH)_{0.48}$ exhibits a remarkable electrochemical activity in agreement with the above mentioned statement emphasizing the positive role of titanium vacancies in storing multivalent ions. The first discharge capacity reaches 165 mAh g^{-1} and is further stabilized to 140 mAh g^{-1} upon charging. The reversible capacity progressively increases during the first three subsequent cycles reaching about 155 mAh g^{-1}, corresponding to the intercalation of ~0.23 mole Mg^{2+} per formula unit. This value is approximately six times higher than for TiO_2 and is comparable to the reference electrodes Mo_6S_8 and $Li_4Ti_5O_{12}$.[6,28] The number of Mg^{2+} ions that can be reversibly intercalated matches the concentration of titanium vacancies, as we will discuss below. Upon cycling, the charge-discharge curves present a sloping aspect, emphasizing a solid-solution behavior. The average voltage was 1.0 V vs. Mg^{2+}/Mg, a value comparable to other titanium-based anode materials in Mg batteries, *i.e.* $TiSe_2$ and $Li_4Ti_5O_{12}$.[28,29] However, the electrode showed a large polarization with an average discharge and charge voltage of 0.5 and 1.5 V, respectively. The origin of such a polarization needs to be addressed. Finally, the $Ti_{0.78}\square_{0.22}O_{1.12}F_{0.40}(OH)_{0.48}$ electrode exhibits excellent rate capability (Figure S4a in Supporting Information) and cycling stability under high current densities. Under 150 mA g^{-1}, the electrode maintained a capacity of around 100 mAh g^{-1} after 200 cycles (Figure S4b in Supporting Information**)**. Even under 300 mA g^{-1}, a capacity of around 65 mAh g^{-1} was maintained after 500 cycles (Figure S4c in Supporting Information).

Similar trend was observed for Al^{3+}, with the presence of titanium vacancies enabling to unlock the electrochemical activity of anatase. Stoichiometric TiO_2 showed negligible electrochemical activity *vs.* Al^{3+}/Al with reversible capacity close to 30 mAh.g^{-1} (**Figure 2g)**. Introducing vacancies leads to an increase of the capacity with the first discharge capacity reaching *ca.* 120 mAh.g^{-1} and further decreasing to 90 mAh.g^{-1} upon charging. In contrast to anion $AlCl_4^-$ intercalation in graphite,[9] only a limited number of materials (Mo_6S_8[30], VO_2[31]

and $V_2O_5{}^{32}$) are prone to insert trivalent Al ions. Although the reversible capacity is found to be too low to enable practical applications, the presence of vacancies substantially improves the charge storage capability of anatase providing a new avenue to activate other types of chemical compounds.
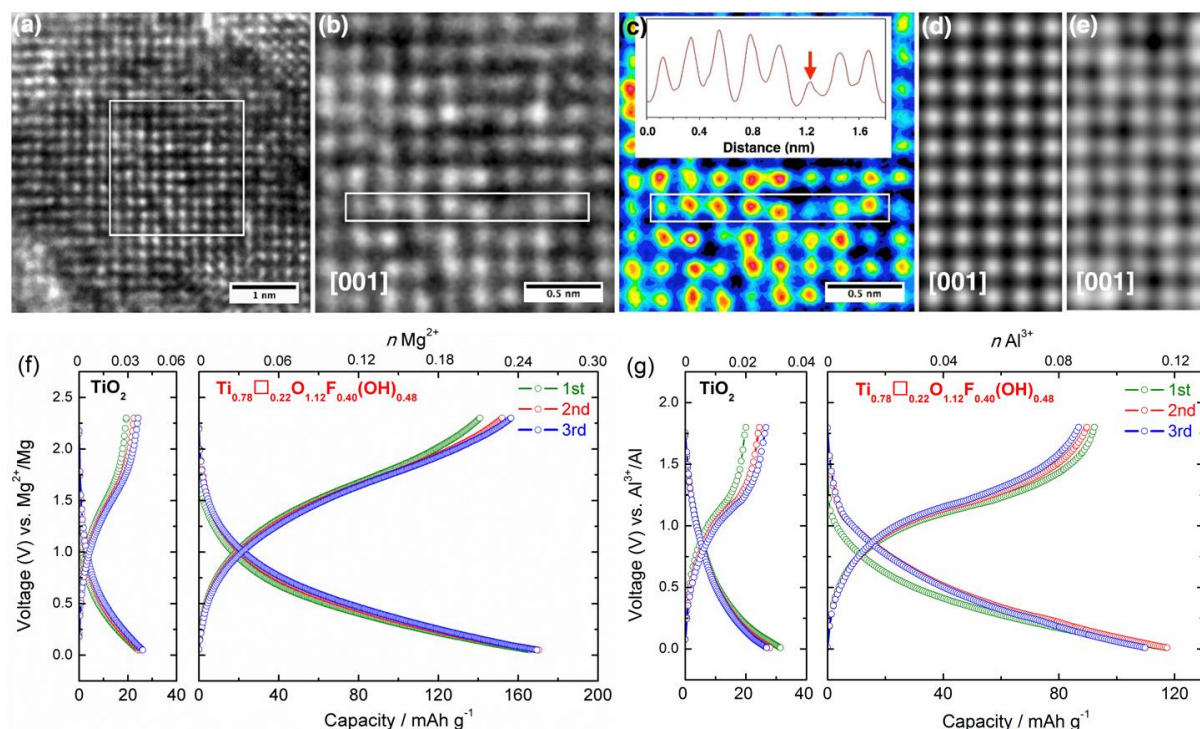

Figure 2. Titanium vacancies enable reversible electrochemical magnesiation/alumination in anatase. (a) High resolution Cs-corrected TEM image of a $Ti_{0.78}\square_{0.22}O_{1.12}F_{0.40}(OH)_{0.48}$ nanoparticle. **(b)** Atomic resolution image of anatase crystal (space group $I4_1/amd$) oriented along the [001] axis. **(c)** Colored HRTEM image with a profile plot of a line of atoms (white rectangle), which exhibit a clear intensity variation both of atomic columns and dark patchs in between. **(d,e)** Calculated high resolution TEM images of anatase structure oriented along [001] axis using MactempasX2 software with an average Ti occupancy of 78%: uniform (d) and random (e) distribution. The calculated image in Figure 1e exhibits similar features that those observed in experimental HR image, which demonstrates the irregularity of the Ti occupancy in the structure. **(f)** Galvanostatic discharge-charge curves for TiO_2 and vacancy containing anatase *vs*. Mg. Cells were cycled under 20 mA g^{-1} in the potential range of 0.05-2.3 V vs. Mg^{2+}/Mg (the electrochemical stability of the electrolyte solution was determined by cyclic voltammetry shown in Figure S2 in Supporting Information). **(g)** Galvanostatic discharge-charge curves for TiO_2 and vacancy containing anatase *vs*. Al. Cells were cycled under 20 mA g^{-1} in the potential range of 0.01-1.8 V vs. Al^{3+}/Al (the electrochemical stability of the electrolyte solution was determined by cyclic voltammetry shown in Figure S3 in Supporting Information).

Detailed analysis of the Mg storage mechanism

Structural analysis on electrochemically magnesiated/de-magnesiated $Ti_{0.78}\square_{0.22}O_{1.12}F_{0.40}(OH)_{0.48}$ electrodes was performed via the pair distribution function (PDF), obtained by Fourier transformation of high-energy x-ray data **(Figure 3a,b)**. This technique

provides diffuse and Bragg intensities and allows structural information to be collected for nanostructured materials.[33] Strikingly, the PDF features show only slight changes upon electrochemical magnesiation and de-magnesiation, emphasizing a robust host framework that undergoes only minor structural changes (**Figure 3b)**. From PDF refinements (Figure S6 and Table S2 in Supporting Information), we monitored the relative change of the lattice constants upon magnesiation **(Figure 3c)** which shows a negligible variation, *i.e.* < 0.6 %. Such "zero-strain" (ΔV < 0.6 %) behavior offers high mechanical stability with respect to repeated cycling.[28]

We considered both octahedral interstitial sites and titanium vacancies as possible hosting sites for the intercalated Mg^{2+} ions. The occupancy of Mg^{2+} in octahedral interstitial sites (4b) and titanium vacancies (4a) obtained by PDF refinements as a function of discharge and charge state is shown in **Figure 3d**. This indicates the selective insertion of Mg^{2+} at titanium vacancies throughout the whole insertion process. Most notably, the discharge capacity matches the number of inserted Mg^{2+} obtained by PDF refinement, consistent with two-electron redox reactions. Upon charge, Mg^{2+} ions are extracted from the titanium vacancies confirming the reversibility of the reaction.
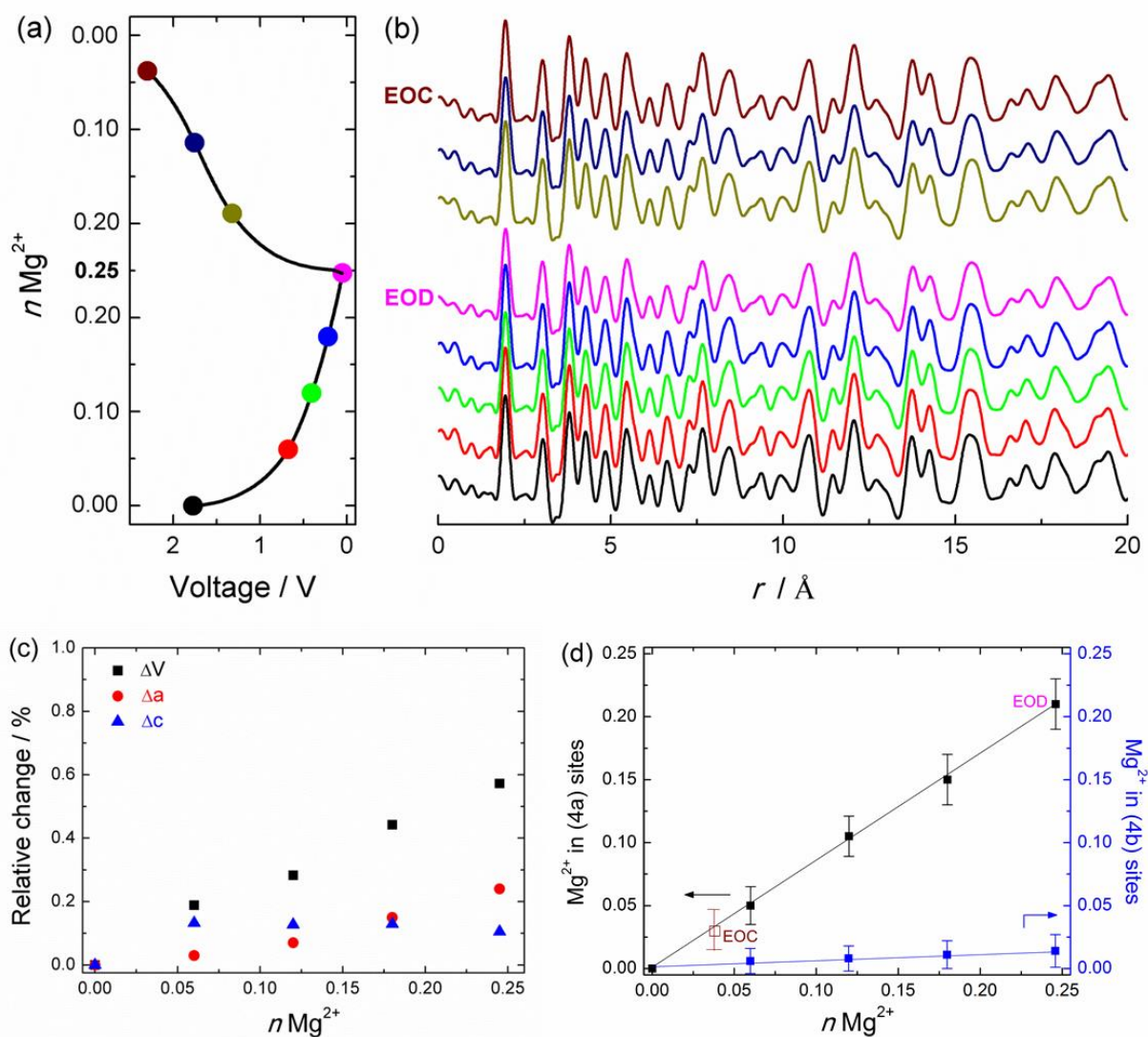
Figure 3. Ex-situ structural analysis of magnesiated/de-magnesiated electrodes. (a,b) Discharge/charge curves with different points selected for ex-situ PDF analysis. EOD and EOC refer to end-of-discharge and end-of-charge, respectively. **(c)** Percentage of relative change of the lattice constants (a, c: unit cell parameters, V: volume) with respect to the initial state of the pristine electrode. **(d)** Mg^{2+} occupancy within the titanium vacancy site (4a) and octahedral interstitial site (4b).

Local spectroscopic analysis of chemically magnesiated sample was performed using EDX and EELS measurements **(Figure 4a,b)** in STEM mode. EDX mapping **(Figure 4a)** was acquired at the K edge of Mg element overlaid with a HAADF-STEM image of the reduced sample. The chemical mapping revealed a heterogeneous localization of Mg atoms in agreement with a random Ti vacancies distribution. EELS-STEM spectra **(Figure 4b)** shows two double peaks corresponding to the edges L_2 and L_3 of Ti element. The intensity ratio of L_2 and L_3 provides information about the valence state of Ti (see Supporting Information for calculation details and Figure S7).[34] Based on this method, the occurrence of Ti^{III} in the reduced sample was clearly established. The rate of Ti^{III} was estimated at 32 % yielding

9

$Mg_{0.13}Ti^{IV}_{0.52}Ti^{III}_{0.26}\square_{0.09}O_{1.12}F_{0.40}(OH)_{0.48}$ (assuming that Mg^{2+} ions occupy only Ti vacancies). Moreover, the EELS-STEM map **(Figure 4e)** of this L_2/L_3 ratio exhibits a clear inhomogeneity in term of degree of oxidation, which is consistent with a random distribution of Ti vacancies.

Further local information was obtained from ^{19}F solid-state NMR spectroscopy. **Figures 4f,g** show the ^{19}F MAS NMR spectra of pristine sample $Ti_{0.78}\square_{0.22}O_{1.12}F_{0.40}(OH)_{0.48}$ and chemically magnesiated sample $Mg_{0.13}Ti^{IV}_{0.52}Ti^{III}_{0.26}\square_{0.09}O_{1.12}F_{0.40}(OH)_{0.48}$. The fluorine environments $Ti^{IV}\square_2$-F, $Ti^{IV}_2\square$-F and Ti^{IV}_3-F have been previously identified in the pristine compound at isotropic chemical shift (δ_{iso}) values equal to 98, -4 and -88 ppm, respectively[20] **(Figure 4f)**. The ^{19}F NMR spectrum of the magnesiated sample (**Figure 4g**) reveals the disappearance of the line characteristic of $Ti^{IV}\square_2$-F species and a strong intensity decrease for the resonance assigned to $Ti^{IV}_2\square$-F species. This confirms a filling of the vacancies by Mg^{2+}, and is consistent with our PDF data (Figure S8 and Table S3 in Supporting Information). Concomitantly, a broad resonance appears at ~ -180 ppm. This isotropic chemical shift value is between those for Ti^{III}_2-F environment in TiF_3 (Figure S9 in Supporting Information) and Mg_3-F environment in MgF_2 ([19]F δ_{iso} = -197.3 ppm).[35,36] These observations are consistent with the formation of new fluorine environments with different numbers of surrounding Mg^{2+}, Ti^{IV}, Ti^{III} species and vacancies (Figures S10-11 and Tables S4-6 in Supporting Information). Dipolar coupling interactions between the unpaired electrons of Ti^{3+} and the ^{19}F nuclei account for the broadness of the ^{19}F NMR resonances of the magnesiated sample which also reflects the diversity of the fluorine environments.
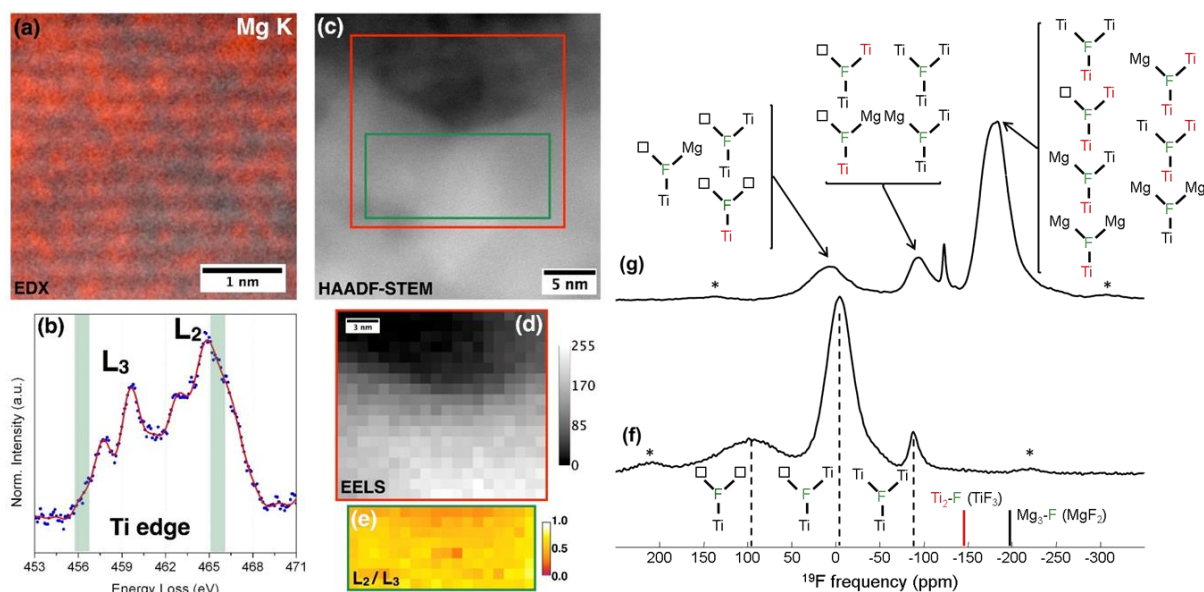
Figure 4. Chemical and local characterizations of Mg^{2+} in anatase. (a) EDX mapping acquired at the K edge of Mg element overlaid with a HAADF-STEM image of Mg$_{0.13}$Ti$_{0.78}\square_{0.09}$O$_{1.12}$F$_{0.40}$(OH)$_{0.48}$. **(b)** EELS-STEM spectra of Mg$_{0.13}$Ti$_{0.78}\square_{0.09}$O$_{1.12}$F$_{0.40}$(OH)$_{0.48}$ exhibiting double peaks corresponding to the edges L2 and L3 of Ti element after the background subtraction. The ratio of the integration of both green areas (L3 for Ti^{III} and L2 for Ti^{IV}) provides information about the degree of oxidation of Ti. **(c)** High resolution STEM image acquired in HAADF mode of Mg$_{0.13}$Ti$_{0.78}\square_{0.22}$O$_{1.12}$F$_{0.40}$(OH)$_{0.48}$. **(d)** EELS-STEM mapping of the red square area in HAADF-STEM image with a loss energy range from 400 to 500 eV. **(e)** Based on the EELS spectrum and the associated map, the mapping of the L2/L3 ratio is obtained exhibiting the strong inhomogeneity of the oxidation degrees of Ti, which is consistent with Ti occupancy distribution. Experimental ^{19}F solid-state MAS NMR spectra of **(f)** Ti$_{0.78}\square_{0.22}$O$_{1.12}$F$_{0.40}$(OH)$_{0.48}$ (60 kHz) and **(g)** chemically magnesiated sample Mg$_{0.13}$Ti$_{0.78}\square_{0.09}$O$_{1.12}$F$_{0.40}$(OH)$_{0.48}$ (34 kHz). The asterisks indicate the main spinning sidebands. The dashed lines indicate the ^{19}F δ_{iso} values of Ti$^{IV}_3$−F, Ti$^{IV}_2\square$−F, and Ti$\square_2$−F environments in Ti$_{0.78}\square_{0.22}$O$_{1.12}$F$_{0.40}$(OH)$_{0.48}$. Solid lines indicate the ^{19}F δ_{iso} values of Ti$^{III}_2$−F environment in TiF$_3$ and Mg$_3$−F environment in MgF$_2$. The arrows indicate the tentative assignment of the NMR resonances to the various species in the chemically magnesiated sample (Ti^{IV} are in black and Ti^{III} are en red). Fits of these spectra are given as supporting information (Figures S10-11, Tables S4 and S6).

Based on these results, we interpret the Mg^{2+} storage mechanism as insertion at titanium vacancies, with a Ti^{4+}/Ti^{3+} redox couple. The insertion reaction can be expressed as

(Ti$^{IV}_{0.78}\square_{0.22}$)$^{[4a]}O_{1.12}F_{0.40}(OH)_{0.48}$ + xMg^{2+} + 2xe$^-$ → (Ti$^{IV}_{0.78-2x}$Ti$^{III}_{2x}\square_{0.22-x}Mg_x$)$^{[4a]}O_{1.12}F_{0.40}(OH)_{0.48}$ (1).

The theoretical capacity based on Eq. (1) is 166 mAh g^{-1}, which is close to the 155 mAh g^{-1} observed reversible capacity. Because the charge storage capacity depends on the concentration of titanium vacancies, the maximum charge storage capacity of this material

can be optimized opening a new approach for the development of electrode materials for multivalent batteries.

To further understand the kinetic aspects of Mg^{2+} diffusion, we extracted the diffusion coefficient as a function of the depth of discharge, using the galvanostatic intermittent titration technique (GITT).[37,38] A concentration dependence of the Mg diffusion coefficient is observed (**Figure 5**), which is characteristic of an intercalation compound featuring vacancy-mediated diffusion.[39] The Mg diffusion can be separated into two domains. The first and second region displayed an average diffusion coefficient of about 9.10^{-17} and 4.10^{-18} cm^2 s^{-1}, respectively. These values are comparable to the lithium diffusion coefficient in anatase nanoparticles (7 nm), *i.e.* 6.2×10^{-17} cm^2 s^{-1}.[40] According to the NMR data, the $Ti\square_2$-F and $Ti_2\square_1$-F environments are present at relative proportions of 33 and 67 % (Table S5). Strikingly, the relative proportions of Mg^{2+} inserted within the first (33 %) and second (67 %) region match the relative proportions of double and single vacancy fluorine environments. According to DFT calculations, the insertion of Mg is more favorable into the paired vacancies system than the single one. Hence, it can be concluded that magnesiation first occurs in one of the paired vacancies before filling the single one, and we assigned the two domains observed in Figure 4a to the diffusion of Mg^{2+} via $Ti\square_2$-F and $Ti_2\square_1$-F/$TiMg\square_1$-F species.

In anatase TiO_2, the Mg diffusion coefficient rapidly decreases with increasing Mg concentration showing that Mg intercalation is kinetically limited. Our calculation result, that Mg intercalation into stoichiometric anatase TiO_2 is energetically favorable (in the dilute limit) is consistent with previous studies.[24] It is, however, possible that thermodynamic factors also hamper Mg intercalation into anatase at higher Mg concentrations. An additional DFT calculation for a supercell containing two Mg^{2+} ions at adjacent interstitial octahedra, however, gave an intercalation energy very close to that of a single isolated Mg ($\Delta E = {}^{-}1.00$ eV per Mg), suggesting that direct Mg–Mg repulsion is not a significant thermodynamic factor, supporting our supposition that this is a kinetic limitation.
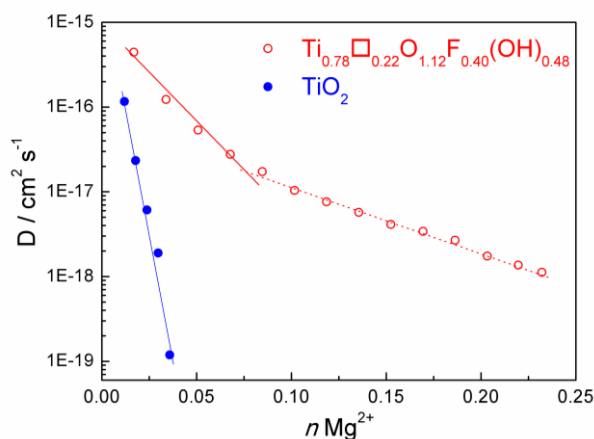
Figure 5. Vacancy mediated diffusion mechanism of Mg^{2+} in anatase. Evolution of diffusion coefficient of Mg^{2+} in anatase TiO_2 and in $Ti_{0.78}\square_{0.22}O_{1.12}F_{0.40}(OH)_{0.48}$ as a function of the discharge depth.

In this work, we have demonstrated that the introduction of titanium vacancies provides a thermodynamically favorable driving force to insert multivalent cations such as Mg^{2+} and Al^{3+} into a textbook compound, anatase TiO_2. The stabilization of new vacant sites that are able to insert multivalent cations allows the kinetically limitation observed in pure stoichiometric anatase to be overcome.

The interstitial site in stoichiometric anatase TiO_2, and the titanium vacancy in F-TiO_2, are both octahedrally coordinated by anions. The interstitial site in TiO_2 is purely oxygen coordinated, while the Ti vacancy in F-TiO_2 has a fluorine rich environment. Such a difference in the anionic environment is expected to induce interaction changes between intercalated cations and the host anionic sublattice. We found that Mg^{2+} and Al^{3+} adopt a five-fold coordination mode in anatase TiO_2 but a six-fold coordination mode in F-TiO_2. Emly and Van der Ven[41] have discussed how higher coordination modes increase the charge redistribution over more titanium–anion bonds, thus lowering the migration barrier of cations. By analogy, we suggest that an increase of the coordination mode of the intercalated species enable an efficient charge redistribution thus contributing to overcome kinetic limiation observed in pure anatase. Moreover, the increase of the coordination mode is accompanied by an increase of the volume of the coordination polyhedra. Comparing the cell volume variations induced by lithium intercalation in pure anatase and Mg in vacancy containing anatase shows that the vacancies mitigate the internal stress induced by the redox process. Based on the Ti^{4+}/Ti^{3+} redox couple, the multiple electron transfer accompanied by the intercalation of multivalent cations achieves similar capacity with half and one-third of

inserted Mg^{2+} and Al^{3+}, respectively, as compared to lithium ions. Hence, for similar capacity, the electrode volume variation is significantly lower.

In the doping strategy described here, the formation of new available vacant sites is accompanied by a proportional decrease in the amount of redox-active transition metal centres, which decreases the theoretical maximum storage capacity. Nevertheless, a small concentration of vacancies can allow a high capacity to be obtained, especially for multi-electron transfer. For example, the full utilization of the titanium vacancies with a three electrons process can yield a capacity of ~250 mAh g^{-1}.

In addition to the enhanced thermodynamically driving force, the observed vacancy mediated diffusion mechanism shows that the high concentration of vacancies removes kinetic limitations. By analogy with the work of Ceder et *al*[42], we surmise that the homogeneous distribution of high concentrations of vacancies creates a percolating network of diffusion pathways that facilitates the diffusion of high-valence cations.

To conclude, we have shown that introducing cationic vacancies unlocks the electrochemical activity of electrode materials towards multivalent cations such as Mg and Al. The use of defect chemistry[43,44] to design advanced electrode materials for multivalent-ion batteries can exploit a large range of materials either starting from structures exhibiting naturally occurring vacancies[45] or synthetically introduced[46].

References

1. Dunn, B., Kamath, H. & Tarascon, J.-M. Electrical Energy Storage for the Grid: A Battery of Choices. *Science* **334**, 928-935 (2011).

2. Armand, M. & Tarascon, J. M. Building better batteries. *Nature* **451**, 652-657 (2008).

3. Tarascon, J. M. & Armand, M. Issues and challenges facing rechargeable lithium batteries. *Nature* **414**, 359-367 (2001).

4. Ponrouch, A., Frontera, C., Barde, F. & Palacin, M. R. Towards a calcium-based rechargeable battery. *Nat. Mater.* **15**, 169-172 (2016).

5. Aurbach, D. *et al.* Prototype systems for rechargeable magnesium batteries. *Nature* **407**, 724-727 (2000).

6. Aurbach, D. *et al.* Progress in Rechargeable Magnesium Battery Technology. *Adv. Mater.* **19**, 4260-4267 (2007).

7. Yoo, H. D. *et al.* Mg rechargeable batteries: an on-going challenge. *Energy Environ. Sci.* **6**, 2265-2279 (2013).

8. Lapidus, S. H. *et al.* Solvation structure and energetics of electrolytes for multivalent energy storage. *Phys. Chem. Chem. Phys.* **16**, 21941-21945 (2014).

9. Lin, M.-C. *et al.* An ultrafast rechargeable aluminium-ion battery. *Nature* **520**, 324-328 (2015).

10. Elia, G. A. *et al.* An Overview and Future Perspectives of Aluminum Batteries. *Adv. Mater.* **28**, 7564-7579 (2016).

11. Ling, C., Banerjee, D. & Matsui, M. Study of the electrochemical deposition of Mg in the atomic level: Why it prefers the non-dendritic morphology. *Electrochim. Acta* **76**, 270-274 (2012).

12. Mohtadi, R. & Mizuno, F. Magnesium batteries: Current state of the art, issues and future perspectives. *Beilstein J. Nanotechnol.* **5**, 1291-1311 (2014).

13. Levi, E., Gofer, Y. & Aurbach, D. On the Way to Rechargeable Mg Batteries: The Challenge of New Cathode Materials. *Chem. Mater.* **22**, 860-868 (2010).

14. Huie, M. M., Bock, D. C., Takeuchi, E. S., Marschilok, A. C. & Takeuchi, K. J. Cathode materials for magnesium and magnesium-ion based batteries. *Coord. Chem. Rev.* **287**, 15-27 (2015).

15. Rong, Z. *et al.* Materials Design Rules for Multivalent Ion Mobility in Intercalation Structures. *Chem. Mater.* **27**, 6016-6021 (2015).

16. Ling, C. & Mizuno, F. Phase Stability of Post-spinel Compound AMn_2O_4 (A = Li, Na, or Mg) and Its Application as a Rechargeable Battery Cathode. *Chem. Mater.* **25**, 3062-3071 (2013).

17. Wagemaker, M., Kentgens, A. P. M. & Mulder, F. M. Equilibrium lithium transport between nanocrystalline phases in intercalated TiO_2 anatase. *Nature* **418**, 397-399 (2002).

18. Borghols, W. J. H. *et al.* The electronic structure and ionic diffusion of nanoscale $LiTiO_2$ anatase. *Phys. Chem. Chem. Phys.* **11**, 5742-5748 (2009).

19. Ren, Y., Hardwick, L. J. & Bruce, P. G. Lithium Intercalation into Mesoporous Anatase with an Ordered 3D Pore Structure. *Angew. Chem. Int. Ed.* **49**, 2570-2574 (2010).

20. Li, W. *et al.* High Substitution Rate in TiO_2 Anatase Nanoparticles with Cationic Vacancies for Fast Lithium Storage. *Chem. Mater.* **27**, 5014-5019 (2015).

21. Su, S. *et al.* A novel rechargeable battery with a magnesium anode, a titanium dioxide cathode, and a magnesium borohydride/tetraglyme electrolyte. *Chem. Commun.* **51**, 2641-2644 (2015).

22. Zhang, M., MacRae, A. C., Liu, H. & Meng, Y. S. Communication—Investigation of Anatase-TiO_2 as an Efficient Electrode Material for Magnesium-Ion Batteries. *J. Electrochem. Soc.* **163**, A2368-A2370 (2016).

23. Liu, S. *et al.* Aluminum storage behavior of anatase TiO_2 nanotube arrays in aqueous solution for aluminum ion batteries. *Energy Environ. Sci.* **5**, 9743-9746 (2012).

24. Legrain, F., Malyi, O. & Manzhos, S. Insertion energetics of lithium, sodium, and magnesium in crystalline and amorphous titanium dioxide: A comparative first-principles study. *J. Power Sources* **278**, 197-202 (2015).

25. Li, W., Body, M., Legein, C., Borkiewicz, O. J. & Dambournet, D. Atomic Insights into Nanoparticle Formation of Hydroxyfluorinated Anatase Featuring Titanium Vacancies. *Inorg. Chem.* **55**, 7182-7187 (2016).

26. Grimaud, A. *et al.* Activation of surface oxygen sites on an iridium-based model catalyst for the oxygen evolution reaction. *Nat. Energy* **2**, 16189 (2016).

27. Wagemaker, M., Borghols, W. J. H. & Mulder, F. M. Large Impact of Particle Size on Insertion Reactions. A Case for Anatase Li_xTiO_2. *J. Am. Chem. Soc.* **129**, 4323-4327 (2007).

28. Wu, N. *et al.* A highly reversible, low-strain Mg-ion insertion anode material for rechargeable Mg-ion batteries. *NPG Asia Mater.* **6**, e120 (2014).

29. Gu, Y., Katsura, Y., Yoshino, T., Takagi, H. & Taniguchi, K. Rechargeable magnesium-ion battery based on a $TiSe_2$-cathode with d-p orbital hybridized electronic structure. *Sci. Rep.* **5**, 12486 (2015).

30. Lee, B. *et al.* Investigation on the Structural Evolutions during the Insertion of Aluminum Ions into Mo_6S_8 Chevrel Phase. *J. Electrochem. Soc.* **163**, A1070-A1076 (2016).

31. Wang, W. *et al.* A new cathode material for super-valent battery based on aluminium ion intercalation and deintercalation. *Sci. Rep.* **3**, 3383 (2013).

32. Le, D. B. *et al.* Intercalation of Polyvalent Cations into V_2O_5 Aerogels. *Chem. Mater.* **10**, 682-684 (1998).

33. Chapman, K. W. Emerging operando and x-ray pair distribution function methods for energy materials development. *MRS Bull.* **41**, 231-240 (2016).

34. Stoyanov, E., Langenhorst, F. & Steinle-Neumann, G. The effect of valence state and site geometry on Ti $L_{3,2}$ and O K electron energy-loss spectra of Ti_xO_y phases. *Am. Mineral.* **92**, 577-586 (2007).

35. Sadoc, A. *et al.* NMR parameters in alkali, alkaline earth and rare earth fluorides from first principle calculations. *Phys. Chem. Chem. Phys.* **13**, 18539-18550 (2011).

36. Baur, W. H. & Khan, A. A. Rutile-type compounds. IV. SiO_2, GeO_2 and a comparison with other rutile-type structures. *Acta Cryst. B* **27**, 2133-2139 (1971).

37. Fattakhova, D., Kavan, L. & Krtil, P. Lithium insertion into titanium dioxide (anatase) electrodes: microstructure and electrolyte effects. *J. Solid State Electrochem.* **5**, 196-204 (2001).

38. Wen, C. J., Boukamp, B. A., Huggins, R. A. & Weppner, W. Thermodynamic and Mass Transport Properties of "LiAl" *J. Electrochem. Soc.* **126**, 2258-2266 (1979).

39. Van der Ven, A., Bhattacharya, J. & Belak, A. A. Understanding Li Diffusion in Li-Intercalation Compounds. *Acc. Chem. Res.* **46**, 1216-1225 (2013).

40. Wang, J., Polleux, J., Lim, J. & Dunn, B. Pseudocapacitive Contributions to Electrochemical Energy Storage in TiO_2 (Anatase) Nanoparticles. *J. Phys. Chem. C* **111**, 14925-14931 (2007).

41. Emly, A. & Van der Ven, A. Mg Intercalation in Layered and Spinel Host Crystal Structures for Mg Batteries. *Inorg. Chem.* **54**, 4394-4402 (2015).

42. Lee, J. *et al.* Unlocking the Potential of Cation-Disordered Oxides for Rechargeable Lithium Batteries. *Science* **343**, 519-522 (2014).

43. Hahn, B. P., Long, J. W. & Rolison, D. R. Something from Nothing: Enhancing Electrochemical Charge Storage with Cation Vacancies. *Acc. Chem. Res.* **46**, 1181-1191 (2013).

44. Kim, H.-S. *et al.* Oxygen vacancies enhance pseudocapacitive charge storage properties of MoO_{3-x}. *Nat. Mater.* **16,** 454-460 (2017).

45. Pernet, M., Strobel, P., Bonnet, B., Bordet, P. & Chabre, Y. Structural and electrochemical study of lithium insertion into γ-Fe$_2$O$_3$. *Solid State Ion.* **66**, 259-265 (1993).

46. Gao, P. *et al.* The critical role of point defects in improving the specific capacitance of δ-MnO$_2$ nanosheets. *Nat. Commun.* **8**, 14559 (2017).

Author contributions

J.M., P.S. and D.D. conceived and coordinated the study. T.K., J.M., M.B., C.L., W.D., M.G., A.D., O.J.B., K.W.C., F.D., H.G., P.S. and D.D.: experimental work and data analysis. B.J.M. and M.S.: computational study. All authors discussed the results and commented on the manuscript. J.M. and D.D. wrote the manuscript with the contribution of all co-authors.

Methods

Synthesis and chemical magnesiation. Ti$_{0.78}\square_{0.22}$O$_{1.12}$F$_{0.4}$(OH)$_{0.48}$ was synthesized using a mild solvothermal process described in our previous report.[20] Briefly, a solution containing 1.2 mL of HF and 24.8 mL of isopropanol was added to 4 mL of titanium isopropoxide in a 45 mL Teflon line container with a fixed ratio of F/Ti setting at 2. After sealing, the solution was heated at 90 °C for 12 hours. After cooling down to room temperature, the white precipitate was separated from the solution using centrifugation and washed several times

with ethanol. The solid was dried at 80 °C overnight, and further outgassed at 150 °C overnight under vacuum. For comparison, anatase TiO_2 was synthesized using the same solvothermal process without HF.

Chemical magnisiation has been performed by using the intercalating agent ethylmagnesium bromide (CH_3CH_2MgBr). Intercalation reactions using ethylmagnesium bromide solution (3.0 M in diethyl ether, Sigma-Aldrich) were carried out by adding the CH_3CH_2MgBr solution drop-by-drop with the excess concentration in diethyl ether to the solid host $Ti_{0.78}\square_{0.22}O_{1.12}F_{0.4}(OH)_{0.48}$ and stirring the mixture for 48 hours at room temperature. The obtained powder was collected by filtration, washed with anhydrous diethyl ether solvent, and dried under vacuum. All subsequent operations were carried out in an argon-filled glove box.

Mg battery electrochemical characterization. The working electrode was composed of 80 wt% active material, 10 wt% conductive carbon (SuperP, Timcal), and 10 wt% polyvinylidene difluoride (PVDF, Aldrich) binder, where active material is either TiO_2 or $Ti_{0.78}\square_{0.22}O_{1.12}F_{0.4}(OH)_{0.48}$. They were suspended in N-methyl-2-pyrrolidone (NMP, Sigma-Aldrich) by hand milling using a mortar, and then drop coated on a Mo foil at the geometrical active mass density of 2 mg cm^{-2}. 0.2 mol L^{-1} 2PhMgCl-AlCl$_3$/THF was used as the electrolyte, and borosilicate glass-fiber filter paper (Whatmann grade GF/A) was used as the separator. Mg metal (99.9%, Good fellow) was used as the reference electrode and the counter electrode. Electrochemical measurements were carried out at 25 ^{o}C using a three-electrode Swagelok-type cell assembled in an argon-filled glove box. Galvanostatic discharge-charge measurements at different current densities in the potential range of 0.05-2.3 V vs. Mg^{2+}/Mg were performed, and the specific capacities were calculated based on the mass of the active material within the electrode. Diffusion coefficient was estimated using galvanostatic intermittent titration technique (GITT).[37,38] GITT measurements were carried out after single discharge-charge cycle. A constant-current discharge pulse of 10 mA g^{-1} was applied to a cell for 1 h followed by a relaxation potential measurement for 10 h. Potential variation (dE^{ocp}/dt) after 10 h was smaller than 5 mV h^{-1}, and this protocol was repeated until the cell potential reached 0.05 V vs. Mg^{2+}/Mg.

Al battery electrochemical characterization. The working electrode was composed of 80 wt% active material, 10 wt% conductive carbon (Super P, Timcal), and 10 wt% polytetrafluoroethylene (PTFE, 60 wt % dispersion in water, Aldrich) binder, where active material is either TiO_2 or $Ti_{0.78}\square_{0.22}O_{1.12}F_{0.4}(OH)_{0.48}$. They were suspended in Milli-Q water by hand milling using a mortar, and then drop coated on a glassy carbon plate (HTW Germany) at the geometrical active mass density of 2 mg cm^{-2}. Al wire (>99.99%, Aldrich),

and Al metal plate (99.99%, Alfa Aesar) were used as the reference electrode, and the counter electrode. A chloroaluminate based room-temperature ionic liquid ([EMIm]Cl-AlCl$_3$) was used as the electrolyte. It was prepared by slowly mixing 1-ethyl-3-methylimidazolium chloride ([EMIm]Cl, 98%, Aldrich) and anhydrous AlCl$_3$ (99.99%, Ultra-dry, Alfa Aesar) under stirring condition by the mole ratio of 1:1.1 in an argon-filled glove box. [EMIm]Cl was dried at 120 °C under the vacuum (< 1 Pa) for 12 h prior to use. Borosilicate glass-fiber filter paper (Whatmann grade GF/D) was used as the separator. Electrochemical measurements were carried out at 25 °C using a three-electrode Swagelok-type cell assembled in an argon-filled glove box. Galvanostatic discharge-charge measurements in the potential range of 0.01-1.8 V vs. Al^{3+}/Al were performed by using Biologic MPG-2 system, and the specific capacities were calculated based on the mass of the active material within the electrode.

Electron microscopy (STEM-EELS). High-resolution TEM experiments were acquired using a JEOL-ARM200F 200 kV equipped of a Cs image corrector and a Cold-FEG. TEM images have been processed using FIJI and Digital Micrograph softwares. HR-TEM images were calculated using the MactempasX-2 software. EDX-STEM and EELS-STEM analyses were acquired using a FEI-TITAN 80-300 kV with ChemiSTEM capability (Cs probe corrector and X-FEG). EELS experiments were carried out on a post-column energy filter system (Gatan Tridiem 865 ER) operated at 80 kV. The processing of the EELS spectrum images was carried out using Hyperspy multidimensional data analysis (https://doi.org/10.5281/zenodo.240660).

Ex-situ synchrotron X-ray scatting characterization. To obtain an insight picture of Mg intercalation/deintercalation process during the entire electrochemical reaction, the Swagelok cells with active electrode materials at different discharged and charged states were disassembled in the glove box and the electrodes were washed by tetrahydronfuran (THF) to remove the residuals. After evacuating the THF, the active materials were scraped off from Mo foil, loaded inside in the Kapton capillaries and sealed in the Argon-filled glove box to avoid exposing to air for the high energy synchrotron X-ray scatting characterization, and data were collected at the starting electrode and the electrodes recovered in various discharged and charged states.

The chemically magnisiated sample was loaded inside in the Kapton capillaries and sealed in the Argon-filled glove box to avoid exposing to air for synchrotron X-ray scatting characterization.

For pair distribution function (PDF) analysis, X-ray scattering data, from which it would be suitable to obtain the PDF data, were measured at the 11-ID-B beamline at the Advanced Photon Source located at Argonne National Laboratory. Synchrotron diffraction data were collected using high energy X-rays (λ = 0.2128 Å) allowing high values of momentum transfer.[47,48] One-dimensional diffraction data were obtained by integrating the diffraction images within fit2D.[49] The G(r) function was extracted from the data following Fourier transformation using PDFgetX2,[50] after correcting for background and Compton scattering. The refinement of the PDF data was performed using the PDFgui software.[51] Refined parameters were the instrument parameters, the lattice parameters, the atomic displacement parameters, the anion position, the cationic site occupancy, and the Mg occupancy.

^{19}F solid-state MAS NMR spectroscopy. Experimental details about the ^{19}F solid-state magic angle spinning (MAS) NMR spectrum of $Ti_{0.78}\square_{0.22}O_{1.12}F_{0.40}(OH)_{0.48}$ have been reported previously.[20] ^{19}F solid-state MAS NMR experiments on chemically magnesiated sample and TiF_3 were performed on a Bruker Avance III spectrometer operating at 7.0 T ([19]F Larmor frequency of 282.2 MHz), using a 2.5 mm CP-MAS probehead. Samples were kept in a dry glove box under nitrogen atmosphere and the rotors were filled inside the glove box to avoid any hydration of the samples. As the samples are paramagnetic, all spectra were recorded at high spinning frequencies ($\geq$ 30 kHz) to enhance the sensitivity and resolution.[52] ^{19}F MAS NMR spectra were acquired using one pulse sequence. The 90° pulse length was set to 1.75 µs and the recycle delay to 20 s (2 s for TiF_3). Depending on the samples and sequences, between 128 and 512 scans were accumulated. Isotropic peaks were discriminated from spinning sidebands by comparing spectra acquired at two spinning frequencies (30 and 34 kHz). Due to air frictional heating, the sample temperature increases with the spinning frequency. [207]Pb isotropic chemical shift of $Pb(NO_3)_2$ was used as a NMR thermometer.[53,54] ^{19}F MAS NMR spectra are referenced to $CFCl_3$ and they were fitted with the DMFit software,[55] using, as for diamagnetic systems, four parameters: the isotropic chemical shift, δ_{iso} (ppm) = $(\delta_{xx} + \delta_{yy} + \delta_{zz})/3$, the chemical shift anisotropy (CSA), δ_{csa} (ppm) = $\delta_{zz} - \delta_{iso}$, the asymmetry parameter, $\eta_{csa} = |\delta_{yy} - \delta_{xx}|/ \delta_{csa}$, and the Gaussian-Lorentzian shape factor. The principal components of the chemical shift tensor are defined in the sequence $|\delta_{zz} - \delta_{iso}| \geq |\delta_{xx} - \delta_{iso}| \geq |\delta_{yy} - \delta_{iso}|$. Hyperfine interactions between the unpaired electrons and the studied nucleus are not explicitly considered in these fits.

Density functional theory (DFT) calculations. Density functional theory (DFT) calculations were performed using the plane-wave code VASP,[56,57] with valence electrons described by a plane-wave basis with a cutoff of 500 eV. Interactions between core and valence electrons

were described with the PAW method,[58] with cores of [Ar] for Ti, [He] for O, [He] for F, [He] for Li, [Ne] for Mg, and [He] for Al. The calculations used the revised Perdew-Burke-Ernzerhof generalized gradient approximation PBEsol,[59] supplemented with a Dudarev $+U$ correction applied to the Ti d states (GGA+U). We used a value of $U_{Ti,d} = 4.2$ eV, which has previously been used to model lithium intercalation in anatase TiO_2 and TiO_2(B).[60-62] To model intercalation into stoichiometric anatase, we first performed a full geometry optimization on a 3×3×1 anatase TiO_2 supercell (108 atoms). Optimised lattice parameters were obtained from a series of constant volume relaxations, with the resulting data fitted to the Murnaghan equation of state. X=(Li, Mg, Al) intercalation was modelled with a single inserted ion at an interstitial site (XTi$_{36}$O$_{72}$). To model intercalation into Ti$_{0.78}$□$_{0.22}$O$_{1.12}$F$_{0.40}$(OH)$_{0.48}$, we considered both a [V_{Ti}+4F$_O$] vacancy complex, and a [2V_{Ti}+8F$_O$] paired vacancy complex, where the vacancies occupy [100]-aligned adjacent Ti sites. Both structures have the maximum possible number of F$_O$ in the same (001) plane as the vacancies, i.e. in equatorial sites for the coordination octahedra. These configurations have previously been shown from DFT calculations to be the most stable for each stoichiometry.[22] Single vacancy calculations used a parent 3×3×1 anatase supercell, and paired vacancy calculations used a parent 4×4×2 anatase supercell. Vacancy intercalation calculations used the same optimized lattice parameters as the stoichiometric 3×3×1 cell. Individual calculations were considered geometry optimized when all atomic forces were smaller than 0.01 eV Å^{-1}. All calculations were spin polarized, and used a 2×2×2 Monkhorst-Pack grid for sampling k-space for the 3×3×1 cells, and a 1×1×1 grid for the 4×4×2 cells. To calculate intercalation energies, reference calculations for the corresponding metallic bulks were performed using the same convergence criteria as above. We considered 2 atom cells for Li and Mg, and a 4 atom cell for Al, with 16×16×16 Monkhorst-Pack grids for k-space sampling. A data set containing the calculation inputs and outputs, and the analysis scripts for calculating the intercalation energies is available at the University of Bath Data Archive.[63]

Data availability. The source data necessary to support the findings of this paper are available from the corresponding author upon request. Supporting data for the computational work described in this study is available as Ref. 63, published under the CC-BY-SA-4.0 license. This repository contains (1) the complete DFT dataset used to support the findings of this study; (2) a Python script for collating the relevant data; (3) a Jupyter notebook containing all computational data analysis. (2) & (3) use the `vasppy` Python module, available under the MIT license.[64]

References

47. Chupas, P. J. *et al.* Rapid-acquisition pair distribution function (RA-PDF) analysis. *J. Appl. Crystallogr.* **36**, 1342-1347 (2003).

48. Chupas, P. J., Chapman, K. W. & Lee, P. L. Applications of an amorphous silicon-based area detector for high-resolution, high-sensitivity and fast time-resolved pair distribution function measurements. *J. Appl. Crystallogr.* **40**, 463-470 (2007).

49. Hammersley, A. P., Svensson, S. O., Hanfland, M., Fitch, A. N. & Hausermann, D. Two-dimensional detector software: From real detector to idealised image or two-theta scan. *High Pressure Res.* **14**, 235-248 (1996).

50. Qiu, X., Thompson, J. W. & Billinge, S. J. L. PDFgetX2: a GUI-driven program to obtain the pair distribution function from X-ray powder diffraction data. *J. Appl. Crystallogr.* **37**, 678 (2004).

51. Farrow, C. L. *et al.* PDFfit2 and PDFgui: computer programs for studying nanostructure in crystals. *J. Phys.: Condens. Matter.* **19**, 335219 (2007).

52. Ishii, Y., Wickramasinghe, N. P. & Chimon, S. A New Approach in 1D and 2D ^{13}C High-Resolution Solid-State NMR Spectroscopy of Paramagnetic Organometallic Complexes by Very Fast Magic-Angle Spinning. *J. Am. Chem. Soc.* **125**, 3438-3439 (2003).

53. van Gorkom, L. C. M., Hook, J. M., Logan, M. B., Hanna, J. V. & Wasylishen, R. E. Solid-state lead-207 NMR of lead(II) nitrate: Localized heating effects at high magic angle spinning speeds. *Magn. Reson. Chem.* **33**, 791-795 (1995).

54. Bielecki, A. & Burum, D. P. Temperature Dependence of ^{207}Pb MAS Spectra of Solid Lead Nitrate. An Accurate, Sensitive Thermometer for Variable-Temperature MAS. *J. Magn. Reson., Ser. A* **116**, 215-220 (1995).

55. Massiot, D. *et al.* Modelling one- and two-dimensional solid-state NMR spectra. *Magn. Reson. Chem.* **40**, 70-76 (2002).

56. Kresse, G. & Hafner, J. Norm-conserving and ultrasoft pseudopotentials for first-row and transition elements. *J. Phys.: Condens. Matter.* **6**, 8245 (1994).

57. Kresse, G. & Furthmüller, J. Efficiency of ab-initio total energy calculations for metals and semiconductors using a plane-wave basis set. *Comput. Mater. Sci.* **6**, 15-50 (1996).

58. Kresse, G. & Joubert, D. From ultrasoft pseudopotentials to the projector augmented-wave method. *Phys. Rev. B* **59**, 1758-1775 (1999).

59. Perdew, J. P. *et al.* Restoring the Density-Gradient Expansion for Exchange in Solids and Surfaces. *Phys. Rev. Lett.* **100**, 136406 (2008).

60. Morgan, B. J. & Watson, G. W. GGA +U description of lithium intercalation into anatase TiO$_2$. *Phys. Rev. B* **82**, 144119 (2010).

61. Morgan, B. J. & Watson, G. W. Role of Lithium Ordering in the Li$_x$TiO$_2$ Anatase $\rightarrow$ Titanate Phase Transition. *J. Phys. Chem. Lett.* **2**, 1657-1661 (2011).

62. Morgan, B. J. & Madden, P. A. Lithium intercalation into TiO$_2$(B): A comparison of LDA, GGA, and GGA+U density functional calculations. *Phys. Rev. B* **86**, 035147 (2012).

63. Morgan, B. J. *et al.,* Computational Dataset for "Reversible Magnesium and Aluminium-ions Insertion in Cation-Deficient Anatase TiO$_2$", *University of Bath Research Data Archive*, http://researchdata.bath.ac.uk/id/eprint/397, doi:10.15125/BATH-00397.

64. Morgan, B. J., "`vasppy` - a Python suite for manipulating VASP files", https://github.com/bjmorgan/vasppy, doi:10.5281/zenodo.801663.